Increased thermostability of an engineered flavin-containing monooxygenase to remediate trimethylamine in fish protein hydrolysates

Marianne Goris[1], Isabel Cea-Rama[2], Pål Puntervoll[1], Rasmus Ree[1], David Almendral[3], Julia Sanz-Aparicio[2], Manuel Ferrer[3], Gro Elin Kjæreng Bjerga[1*]

1. NORCE Norwegian Research Centre, Bergen, Norway
2. Instituto de Quimica Fisica Rocasolano (IQFR), CSIC, Madrid, Spain
3. Instituto de Catalisis y Petroleoquimica (ICP), CSIC, Madrid, Spain

* Corresponding author; e-mail: gro.bjerga@norceresearch.no; postal address: Gro Bjerga, NORCE Norwegian Research Centre, Thormøhlens gate 55, N-5008 Bergen, Norway

Running title: Thermostable trimethylamine monooxygenase

Abstract

Protein hydrolysates made from marine by-products are very nutritious, but frequently contain trimethylamine (TMA) which has an unattractive fish-like smell. Bacterial trimethylamine monooxygenases can oxidize TMA into the odorless trimethylamine *N*-oxide (TMAO) and have been shown to reduce TMA-levels in a salmon protein hydrolysate. To make the *Methylophaga aminisulfidivorans* trimethylamine monooxygenase, mFMO, more suitable for industrial application, we engineered it using the Protein Repair One-Stop Shop (PROSS) algorithm. All seven mutant variants, containing 8-28 mutations, displayed increases in melting temperature between 4.7 °C and 9.0 °C. The crystal structure of the most thermostable variant, mFMO_20, revealed the presence of four new stabilizing interhelical salt bridges, each involving a mutated residue. Finally, mFMO_20 significantly outperformed native mFMO in its ability to reduce TMA levels in a salmon protein hydrolysate at industrially relevant temperatures.

Importance

Marine by-products are a high-quality source for peptide ingredients, but the unpleasant fishy odour caused by TMA limits their access to the food market. This problem can be mitigated by enzymatic conversion of TMA into the odourless TMAO. Enzymes isolated from nature must be adapted to industrial requirements, however, such as the ability to tolerate high temperatures. This study has demonstrated that mFMO can be engineered to become more thermostable. Moreover, unlike the native enzyme, the best thermostable variant efficiently oxidized TMA in a salmon protein hydrolysate at

industrial temperatures. Our results present an important next step towards application of this novel and highly promising enzyme technology in marine biorefineries.

Key words: Flavin-containing monooxygenases, trimethylamine, protein hydrolysate, enzyme engineering, PROSS

48 ## Introduction

49 Flavin containing monooxygenases (FMOs, EC 1.14.13.8) are enzymes that insert one
50 molecule of oxygen into organic substrates using the cofactors FAD and NAD(P)H
51 (Ceccoli et al., 2014; Torres Pazmiño et al., 2010; van Berkel et al., 2006). A subgroup
52 of bacterial FMOs oxidize trimethylamine (TMA) to trimethylamine *N*-oxide (TMAO)
53 and are often referred to as trimethylamine monooxygenases (Tmms) (Chen et al., 2011;
54 Choi et al., 2003; Goris et al., 2020). These and other FMOs have also gained interest
55 for their ability to convert indole into the dye indigo and the drug agent indirubin (Choi
56 et al., 2003; Fabara and Fraaije, 2020; Han et al., 2012; Rioz-Martínez et al., 2011).
57 TMA is a well-known contributor to the odor of spoiled fish (Hebard et al., 1982), and
58 may accumulate to give rise to a strong bodily odor in humans with trimethylaminuria
59 (fish odor syndrome) caused by impairments in the *FMO3* gene (Schmidt and Leroux,
60 2020).
61
62 Fish protein hydrolysates made from by-products from fisheries and aquaculture are of
63 high nutritional value, and have a great potential for the human consumption market
64 (Shavandi et al., 2019; Villamil et al., 2017). However, fish protein hydrolysates
65 frequently suffer from an off-putting malodor which is mainly caused by TMA.
66 Currently, the TMA malodor may be handled by odor masking, vaporization,
67 encapsulation or filtration, albeit with varying degrees of success and possibly also
68 compromising other qualities in the products. Application of Tmm enzymes is thus an
69 alternative and novel strategy to convert TMA to the odorless TMAO in fish protein
70 hydrolysates. This has the potential to significantly improve the organoleptic quality of

71 fish protein hydrolysates and thereby promoting their application as food ingredients,
72 while simultaneously maintaining their nutritional profile.
73
74 In a previous study, we screened 45 bacterial Tmms for their ability to oxidize TMA to
75 TMAO (Goris et al., 2020), and identified the *Methylophaga aminisulfidivorans* Tmm
76 (mFMO) (Choi et al., 2003) as a suitable candidate for application on a TMA-
77 containing salmon protein hydrolysate. In industrial fish protein hydrolysis, enzymes
78 are required to perform at pH around 6 and temperatures ranging from 45 °C to 60 °C
79 (Aspevik et al., 2016; Kristinsson and Rasco, 2000). This implies that mFMO, with an
80 optimal temperature of 44.0 °C and melting temperature of 46.7 °C, would benefit from
81 enzyme engineering to increase its stability (Goris et al., 2020). In that respect, a
82 previous effort to engineer mFMO is encouraging. Lončar and colleagues used the
83 computational protocol FRESCO (Lončar et al., 2019; Wijma et al., 2018) to predict
84 two mutations in a mFMO, M15L and S23A, that when combined increased the
85 apparent melting temperature by 3.0 °C (Lončar et al., 2019).
86
87 The mFMO enzyme forms a dimer and each monomer consists of two domains: the
88 larger FAD-binding domain and the smaller NADPH-binding domain (Alfieri et al.,
89 2008; Cho et al., 2011). Upon binding, NADPH reduces the tightly bound FAD, thus
90 generating the reactive flavin intermediate C4a-hydroperoxy-FAD and $NADP^+$. The
91 latter stabilizes the activated flavin intermediate, and together with residue tyrosine 207,
92 it shields the active site and the intermediate from the solvent (Alfieri et al., 2008).
93 When entering the active site, the substrate displaces $NADP^+$ and is subsequently
94 oxidized by the activated flavin intermediate.

Protein Repair One-Stop Shop (PROSS) is a web server that takes a protein structure as input and outputs several mutated sequences that are expected to have increased stability (Goldenzweig et al., 2016). PROSS combines multiple independently stabilizing mutations by integrating Rosetta modelling and phylogenetic sequence information (Goldenzweig et al., 2016). In a recent community-wide experimental evaluation of PROSS, designs for nine of ten tested protein targets displayed increased temperature stability, ranging from 8.3 °C to 27.0 °C (Peleg et al., 2021).

In the present study, we employed the PROSS algorithm on mFMO to improve its thermal stability. Seven combinatorial mutant variants of mFMO, containing 8-28 mutations, were analyzed for their temperature stability and compared to wild type mFMO. We demonstrate that all mFMO variants were more thermostable than the wild type. The most thermostable variant was analysed by steady state kinetics and compared to the wild type without identifying substantial modification of the kinetic parameters. Moreover, this stabilized mFMO variant also converted TMA to TMAO more efficiently than native mFMO in a salmon protein hydrolysate at two industrially relevant temperatures, 50.0 °C and 65.0 °C. Finally, the crystal structure of the most thermostable variant was solved to elucidate the structural basis for the increased thermal stability, revealing loss of flexibility through a novel network of polar interactions as the main contributing factor.

Results

118 **Design and expression of mutant variants of mFMO with predicted increased**
119 **stability**
120 To make a more stable and temperature resistant mFMO, ideally withstanding at least
121 50 °C in industrial applications, we employed computational enzyme engineering. The
122 most recent crystal structure of mFMO in complex with the cofactors FAD and $NADP^+$
123 (PDB ID:2XVH) (Cho et al., 2011) was used as input to the PROSS web server
124 (Goldenzweig et al., 2016) along with instructions to exclude residues in contact with
125 the cofactors, as well as dimer interface residues, as mutational targets. PROSS
126 proposed 7 mFMO variants with the number of mutations ranging from 8 to 28 (Figure
127 1, Figure S1). The variants were named mFMO_*n*, where *n* indicates the number of
128 mutations. The mutations were located at or near the surface, and the number of
129 residues predicted to form new stabilizing salt bridges increased from 2 in mFMO_8 to
130 8 in mFMO_28 (Figure 1, Table 1). In the models of mFMO_8 through mFMO_20, all
131 new salt bridges were predicted to form between one mutated and one native residue
132 (Table 1). The last two variants displayed more complex salt bridge patterns: In
133 mFMO_24, the newly introduced N394K mutation is predicted to form salt bridges with
134 both T370D and D374, and in mFMO_28, the newly introduced P391D mutant is
135 predicted to form a third salt bridge with N394K (Table 1). Interestingly, the majority of
136 the new salt bridges are predicted to form interhelical connections (Table 2).
137
138 All 7 mFMO mutant variants were expressed with a C-terminal hexa-histidine tag, at
139 levels comparable to that of native mFMO, purified (Figure S2), and verified by mass
140 spectrometry. When expressing mFMO in *Escherichia coli*, the culture medium turns
141 blue due to the enzymatic conversion of endogenous indole to indigo (Choi et al., 2003;

142 Fabara and Fraaije, 2020; Goris et al., 2020). The fact that the culture media of all
143 mFMO variants turned blue following overnight expression suggested that the
144 expressed mFMO variants were functional. Moreover, all purified mFMO variant
145 enzymes were colored bright yellow, indicating the presence of bound FAD cofactor,
146 which is required for function.
147
148 **mFMO mutant variants are functional and more thermostable than native mFMO**
149 To investigate whether the mFMO variants had increased thermal stability compared to
150 the native enzyme, we conducted protein melting studies using circular dichroism. The
151 melting temperature (T_m) of native mFMO was measured to be 46.2 °C (Table 3), which
152 is in line with previous results (Goris et al., 2020). All mFMO variants demonstrated
153 increased temperature stability compared to the wildtype enzyme, as reflected by their
154 T_m values, which ranged from 50.9 °C for mFMO_28 to 55.2 °C for mFMO_20 (Table
155 3). The melting temperature increased with the number of mutations from mFMO_8 to
156 mFMO_20 but declined slightly for mFMO_24 and mFMO_28.
157
158 To study the increased temperature stability of the mFMO variants further, we evaluated
159 their remaining catalytic activity against TMA after one-hour incubations at
160 temperatures from 30.0 °C to 54.0 °C. The temperature at which half the enzyme
161 activity was lost ($T_{1/2}$) ranged from 45.1 °C for mFMO_8 to 50.0 °C for mFMO_20, all
162 outperforming native mFMO which had a $T_{1/2}$ of 40.6 °C (Table 3). The $T_{1/2}$ values
163 increased with the number of mutations in the same manner as the T_m, with a moderate
164 decline recorded for mFMO_24 and mFMO_28.
165

166 As production of protein hydrolysates is often performed between pH 6.0 and 7.0
167 (Aspevik et al., 2016; Kristinsson and Rasco, 2000), we also assessed whether
168 engineering altered the pH optimum, which was previously determined to be 8.5 for
169 native mFMO (Goris et al., 2020). As seen in Table 3, all mFMO variants had pH
170 optima between 7.5 and 8.0, which are slightly lower than that of native mFMO.
171
172 Although mFMO_20 did not have the lowest pH optimum among the mutant variants, it
173 displayed the greatest improvement in temperature stability, as reflected by both T_m and
174 $T_{1/2}$. As mFMO_20 thus emerged as the most promising variant for industrial
175 application, we determined its optimal temperature (T_{opt}) for enzymatic activity and
176 compared it to that of native mFMO. To determine T_{opt}, we assessed the specific activity
177 against TMA at temperatures between 22 °C and 50 °C, at pH 8.0 (Figure S3). The T_{opt}
178 for both native mFMO and mFMO_20 was found to be 40 °C (Table 3). The T_{opt} for
179 native mFMO was previously reported to be 45 °C (at pH 7.5) (Goris et al., 2020), but
180 the observed differences in the activity measured at 40 and 45 °C in both studies were
181 marginal.
182
183 Engineering enzymes to increase stability often comes with a trade-off of diminished
184 catalytic activity (Klesmith et al., 2017). We therefore performed a steady-state kinetic
185 analysis of native mFMO and mFMO_20, using TMA as substrate with fixed
186 concentrations of NADPH (Table 3). Under the conditions tested, the K_M^{TMA} of native
187 mFMO was 1.07 µM and the k_{cat}^{TMA} was 1.28 s^{-1}. The K_M^{TMA} values of mFMO_20 was
188 0.83 µM and the k_{cat}^{TMA} was 0.93 s^{-1}, both slightly lower than that of native mFMO.

189 Interestingly, the catalytic efficiency (k_{cat}/K_M) of mFMO_20 remained almost identical
190 to that of native mFMO (Table 3).
191
192 **mFMO_20 reduces the TMA level by 95% in salmon protein hydrolysate at 65 °C**
193 Since mFMO_20 demonstrated the most prominent increase in thermal stability, we
194 compared its ability to convert TMA to TMAO in a salmon protein hydrolysate to that
195 of native mFMO. The cofactor NADPH was supplemented, as the hydrolysate did not
196 contain sufficient amounts to drive the enzymatic reaction (Goris et al., 2020). Heat-
197 calibrated enzymes and 0.5 mM NADPH were added to salmon protein hydrolysates
198 (pH 6.1) and incubated for 1 hour at 30 °C, 50 °C and 65 °C, followed by measurements
199 of TMA and TMAO concentrations (Figure 2). When treated with the native enzyme,
200 the TMA level in the hydrolysate was reduced by 52% at 30°C and 46% at 50°C, and
201 only 29% reduction was observed at 65°C. The mutant variant mFMO_20 outperformed
202 native mFMO at all temperature with a striking 95% reduction of TMA at both 50°C
203 and 65°C.
204
205 **Network of novel polar interactions stabilizes mFMO_20**
206 To understand the structural basis for the increased thermostability of mFMO_20, we
207 crystallized it with the cofactors FAD and NADPH. The crystals were indexed in the
208 $C222_1$ space group and contained the biological dimer within the asymmetric unit, with
209 one FAD and one $NADP^+$ molecule bound per catalytic site. The crystal structure of the
210 mFMO_20/FAD/$NADP^+$ complex was solved at 1.62 Å resolution, revealing a structure
211 highly similar to that of native mFMO (PDB ID: 2XVH) (Cho et al., 2011), as reflected
212 by a calculated RMSD of 0.27 Å (on 445 Cα atoms). The small domain contains 4

213 mutations, and the large domain contains the other 16 (Figure 3). Compared to native
214 mFMO, mFMO_20 has a net charge change of -4. Interestingly, half of the mFMO_20
215 mutations are located in a 46-amino-acid subsequence (M353Q-L398K) of a region in
216 the large domain containing three helices: α6 (K345-T361), α7 (A365D-M382), and α8
217 (I390-N406) (Figure 3). Structural analysis revealed that five of these mutated residues
218 form new salt-bridges involving six native residues (K358R-D374, L360E-R356,
219 A365D-K401, N378D-K300-D351, and L398K-E366), of which four form interhelical
220 interactions (Figure 4A, Table 4), thus confirming the PROSS model predictions (Table
221 2). The helices α6 and α7 are directly connected by K358R-D374, and indirectly
222 connected, via the β18-β19 loop, by N378D-K300-D351. The helices α7 and α8 are
223 connected by A365D-K401 and L398K-E366. Two new hydrogen bonds involving side
224 chains were also introduced: one forming an intrahelical bond (α6; M353Q-R356) and
225 the other an interhelical bond (α7-α8; T370D-N394) (Table 4). In addition to the salt
226 bridges directly introduced by mutated residues, mFMO_20 has 4 new salt bridges
227 involving native residues, compared to native mFMO (Figure 4A). All but one of the
228 salt bridges identified in native mFMO were also present in mFMO_20 (Figure 4B).
229 The B-factor profile of mFMO_20 is different from that of native mFMO (Figure 4C
230 and 4D), indicating differences in structural stability and flexibility. The region with the
231 highest B-factor in mFMO_20 is the loop between β-strands 11 and 12, which is located
232 at the entrance of the active site. In contrast, several loops in native mFMO display
233 higher B-factors than that of the β11-β12 loop.
234

235 **Discussion**

236 We have previously shown that mFMO can convert the malodorous TMA molecule into
237 the odorless TMAO in a salmon protein hydrolysate (Goris et al., 2020). To make
238 mFMO more suitable for such industrial applications, which typically takes place at
239 temperatures ranging from 45 °C to 60 °C (Aspevik et al., 2016; Kristinsson and Rasco,
240 2000), we employed the PROSS algorithm to improve its thermal stability. All 7 mutant
241 variants of mFMO were functional enzymes with increased thermostability (Table 3).
242 The best variant was mFMO_20, which displayed the highest increase in temperature
243 stability (Table 3). The crystal structure of mFMO_20 demonstrated that the overall
244 structure of this mutant variant was highly similar to that of native mFMO, but also
245 revealed new structural features that could explain the increased structural stability. The
246 most striking new features were five salt bridges involving mutated residues, of which
247 four formed stabilizing interhelical connecting bridges (Figure 4A). Although PROSS
248 failed to correctly model the intrahelical salt bridge between L360E and R356 and
249 predicted an intrahelical salt bridge between N290D and R292 that was not observed in
250 the crystal structure, all four interhelical salt bridges were correctly modeled (Table 2),
251 thus emphasizing the quality of the PROSS predictions. The only interhelical salt bridge
252 that was present in all 7 PROSS models was the N378D-K300-D351 bridge, which
253 connects α6 to α7 via the β18/β19-loop (Table 2). The N378D mutation leads to the
254 replacement of a hydrogen bond between N378 and K300 in the native mFMO
255 structure, by the stronger salt bridge between N378D and K300, and also induces K300
256 to form a salt bridge with D351, which is not present in the native structure. The fact
257 that the largest increase in temperature stability from one variant to the next was
258 observed going from native mFMO to mFMO_8, and that mFMO_8 only contains one
259 interhelical salt bridge, may suggest that N378D is a key stabilizing mutation. The

260 importance of the additional interhelical salt bridges is also corroborated by the fact that
261 the observed gradual increase in temperature stability from mFMO_8 to mFMO_20
262 coincides with a gradual increase in the number of such bridges from 1 in mFMO_8 to 4
263 in mFMO_20 (Table 2). These results are in line with the recently published
264 community-wide PROSS evaluation, where a correlation between the number of
265 mutations and gain of thermal stability was observed (Peleg et al., 2021). However,
266 despite introducing 4 and 8 more mutations, leading to two more salt bridges predicted
267 to connect secondary structure elements in mFMO_24 (both between α7 and α8) and
268 mFMO_28 (one between α7 and α8 and one between α6 and the β17/β18-loop), the
269 temperature stability of these variants decreased slightly compared to mFMO_20. One
270 possible explanation is that the intricate network of salt bridges in mFMO_24 and
271 mFMO_28, which also involves direct bridges between mutated residues, are
272 incorrectly predicted by PROSS.
273
274 In a previous effort to identify mutations that confer increased thermostability to
275 mFMO, Lončar and colleagues used the FRESCO protocol to predict stabilizing single
276 mutations (Lončar et al., 2019). The FRESCO analysis yielded 140 single mutant
277 candidates that were expressed, purified, and screened for increased thermostability, and
278 14 of these displayed an apparent increase in melting temperature of >1 °C. The two
279 mutations M15L and S23A were combined and the resulting mFMO variant had a 3 °C
280 increase in melting temperature. Adding additional stabilizing single mutations did not
281 further increase thermostability. In line with what we observed with mFMO_20, no
282 major effects were observed on the kinetic parameters of the mFMO M15L/S23A
283 variant. FRESCO has also been used to stabilize the *Rhodococcus* sp. HI-31

284 cyclohexanone monooxygenase (Fürst et al., 2019), which also belongs to the FMO
285 family. In this case, half of the 128 screened single mutant variants had modest
286 stabilizing effects. These were combined, using a shuffled library design strategy, into a
287 variant carrying 8 mutations (M8B), which increased the unfolding temperature by
288 13°C. In contrast to the PROSS mFMO mutant variants, the FRESCO-derived
289 mutations in neither M8B nor mFMO M15L/S23A appear to form new salt bridges.
290
291 We engineered mFMO to make it more suitable for industrial applications, such as
292 removing TMA in salmon protein hydrolysates. The mFMO_20 variant was selected as
293 the best candidate due to it being the most thermostable variant of the seven designs. In
294 addition, the optimal pH for mFMO_20, pH 8.0, was slightly lower than that of native
295 mFMO, pH 8.5, which may also confer an advantage in industrial applications (e.g., the
296 pH of the salmon protein hydrolysate was 6.1). In fact, the optimal pH for all 7 mutant
297 variants was between 7.5 and 8.0 (Table 3), but with no discernable correlation with
298 changes in charge or pI. The optimal temperature of mFMO_20 did not increase
299 compared to native mFMO. Still, this minor disadvantage of mFMO_20 was clearly
300 outweighed by the beneficial properties of increased stability, when tested for its ability
301 to convert TMA to TMAO in the salmon protein hydrolysate (Figure 2). At both 50 °C
302 and 65 °C mFMO_20 was superior to native mFMO in removing TMA, eliminating
303 95% of TMA, and it also appeared to perform best at 30 °C. These results demonstrate
304 that mFMO_20 is indeed more suitable for industrial applications than the native
305 mFMO. However, there are still important hurdles that must be overcome before this
306 Tmm enzyme can be incorporated into an industrial process, especially its dependence
307 on the unstable and expensive cofactor NADPH. The fact that we and others have

308 demonstrated that the Tmms can be engineered opens the possibility for cofactor
309 engineering, which can be used to make the enzyme accept more cost-efficient
310 cofactors. An alternative or complementary strategy is to bring down cost by
311 regenerating the cofactor, e.g., by using glucose dehydrogenase (Mourelle-Insua et al.,
312 2019).
313
314 The current work has demonstrated that the PROSS method successfully predicted
315 mFMO variants with increased thermostability. All 7 variants proposed by PROSS,
316 showed increased thermostability, with comparable properties to engineered FMO
317 enzymes obtained after screening more than 100 single mutant variants followed by
318 library shuffling or rational engineering (Fürst et al., 2019; Lončar et al., 2019). The
319 mFMO_20 variant with its improved stability may be applicable for industrial use as it
320 is because it can reduce the majority of TMA present in fish hydrolysates. It can also
321 serve as an excellent starting point for rational engineering to further improve its
322 catalytic efficiency or for cofactor engineering to make it accept more cost-efficient
323 cofactors.
324

325 Materials and Methods

326 Protein stabilization mutagenesis using the PROSS webserver

327 The Protein Repair One-Stop Shop (PROSS) server (https://pross.weizmann.ac.il/) was
328 used to predict variants of mFMO with increased stability (Goldenzweig et al., 2016).
329 The mFMO structure (PDB ID: 2XVH) (Cho et al., 2011) was used as input and chain
330 A was chosen as design target. To avoid mutating FAD- and NADPH-interacting
331 residues, the small molecule ligands constraint was set to “FAD, NAP”, and to avoid

332 mutating dimer interface residues, the interacting chains constraint was set to "B". The
333 multiple sequence alignment used as basis for the analyses was automatically generated
334 by PROSS using the following default parameters: a minimal sequence identity of 30%,
335 a maximum of 3,000 targets; and an E-value threshold of 0.0001. The PROSS server
336 was accessed 7 October 2019. Salt bridges in the resulting structural models of mFMO
337 variants were identified using the VMD (version 1.9.4) Salt Bridges Plugin (version
338 1.1) with default settings: the oxygen-nitrogen distance cut-off was 3.2 Å and the side-
339 chain centers of mass cut-off was set to none. PyMOL (version 2.4, Schrödinger Inc.,
340 New York, NY, USA was used to confirm the predicted salt bridges involving mutated
341 residues and to visualize the structural models. The multiple sequence alignment of
342 native mFMO and the sequences of the PROSS mutants was visualized using a Python
343 script and combined with the secondary structures of mFMO (PDB ID: 2XVH)
344 visualized using ESPript (version 3.0).
345
346 **Molecular cloning of mFMO variants**
347 The mFMO mutant variants predicted by PROSS were ordered as genes, codon-
348 optimized for expression in *E. coli* and flanked by SapI sites, from TWIST Bioscience
349 (San Francisco, CA, USA). Each mutation was introduced by changing the relevant
350 codon of the native residue to one of the frequently used codons for the mutant residue
351 in the *E. coli*, guided by the Codon Usage Database, and using the gene sequence
352 encoding mFMO optimized for expression in *E. coli* as a starting point (Goris et al.,
353 2020). The genes were subcloned into the C-terminal His-tag containing expression
354 vector pBXC3H (p12) by fragment exchange cloning as previously described (Bjerga et
355 al., 2016; Geertsma and Dutzler, 2011; Goris et al., 2020). Briefly, subcloning was

356 performed using the *E. coli* MC1061 strain and Luria-Bertani (LB)-agar supplemented
357 with ampicillin (100 µg/mL, Sigma-Aldrich, St. Louis, MO, USA) for selection, and the
358 resulting plasmids, purified using the NucleoSpin plasmid kit (Macherey-Nagel, Düren,
359 Germany), were confirmed by sequencing.
360

361 **Protein expression and purification**

362 Native mFMO and mutant variants were expressed and purified essentially as
363 previously described (Goris et al., 2020). Briefly, expression was performed using *E.*
364 *coli* MC1061 cells in 100 mL LB-medium supplemented 100 µg/mL ampicillin at 20 °C
365 for 16 hours after induction with 1% (w/v) L-arabinose. All purification steps were
366 conducted at 4 °C. Cells were harvested by centrifugation, resuspended in lysis buffer,
367 lysed by freeze thaw cycles and sonication, and cleared by centrifugation. The His-
368 tagged mFMO variants were then purified from the cleared lysate using Ni-NTA resin.
369 The buffer of the eluted protein was changed to 50 mM TrisHCl, pH 7.5, 100 mM NaCl
370 using PD10 columns (GE Healthcare, Chicago, IL, USA). Finally, the protein was
371 concentrated using protein concentrator columns (Thermo Fisher, Waltham, MA, USA)
372 and stored with 10% glycerol at -20 °C until further use. Protein concentrations were
373 measured using the Pierce™ 660 nm Protein Assay Reagent (Thermo Fisher) with BSA
374 as standard, and purity was assessed by polyacrylamide gel electrophoresis (SDS-
375 PAGE).
376

377 **Peptide Mass Fingerprinting by Matrix-Assisted Laser Desorption/Ionization-**
378 **Time-of-Flight/Time-Of-Flight (MALDI-TOF/TOF)**

379 MALDI-TOF/TOF analysis in-solution of purified protein samples was performed as
380 previously described (Santiago et al., 2018). The confidence interval for protein
381 identification was set to ≥95% ($p < 0.05$) and only peptides with an individual ion score
382 above the identity threshold were considered correctly identified. The analysis was
383 performed at the Unidad de Proteómica, Centro Nacional de Biotecnología (CNB-
384 CSIC), Madrid, Spain (analysis ID 3408).
385
386 **Enzyme activity assay**
387 Enzyme activity towards TMA was assessed by monitoring the consumption of the
388 cofactor NADPH as previously described (Goris et al., 2020). Briefly, the assay was
389 performed in 96-well microtiter plates, using reaction buffer (50 mM Tris-HCl pH 8.0,
390 100 mM NaCl) supplemented with 0.5 mM NADPH (Merck, Rahway, NJ, USA/Sigma-
391 Aldrich) and 0.01-0.02 mg/mL enzyme. The reactions were initiated by adding 1 mM
392 TMA (Sigma-Aldrich), and consumption of NADPH was measured by continuously
393 monitoring absorbance at 340 nm over 30 minutes using an Epoch™ Microplate
394 Spectrophotometer (Biotek, Winooski, VT, USA). Initial reaction rates were determined
395 from linear fits of the absorbance versus time corrected for blank. Assays were
396 performed in triplicates at 22 °C, unless otherwise stated. One unit (U) of enzyme
397 activity was defined as the number of enzymes required to transform 1 µmol substrate
398 in 1 minute under the stated assay conditions and using the extinction coefficient ε_{340} =
399 6.22 mM^{-1} cm^{-1} for NADPH.
400
401 **pH optimum**

402 pH optimum was measured using the enzyme activity assay as described above, in a
403 three-component buffer (100 mM sodium acetate, 50 mM Bis-Tris and 50 mM Tris)
404 that was pH adjusted using 100% acetic acid. pH dependence was investigated between
405 pH 6.0 and 9.0, with increments of 0.5, and the enzymes were incubated for 2 h in the
406 appropriate buffer at a fixed temperature of 22 °C before measuring residual enzymatic
407 activity by adding NADPH and TMA. The experiment was performed on one biological
408 replicate (enzyme preparation) with technical triplicates.
409
410 **Temperature optimum**
411 Optimal temperature was measured using the enzyme activity assay described above in
412 1 mL cuvettes using a Cary 60 UV-Vis spectrophotometer (Agilent Technologies, Santa
413 Clara, CA, USA) at 22 °C and temperatures from 30 °C to 50 °C with 5 °C increments
414 using a circulating water bath. The enzymes were diluted to 0.01 mg/mL in 1 mL buffer
415 (50 mM Tris-HCl, pH 8.0, 100 mM NaCl) preheated in a water bath to the
416 corresponding temperature and incubated for 1 minute together with 0.5 mM NADPH
417 before initiating the reaction with 1 mM TMA. Two biological replicates (enzyme
418 preparations) were tested, each with 1 to 3 technical replicates resulting in at least three
419 replicates per temperature step for each enzyme. No reliable measurements were
420 obtained for native mFMO at 50 °C.
421
422 **Temperature stability**
423 To assess temperature stability, freshly purified enzymes were diluted to 0.5 mg/mL in
424 reaction buffer (50 mM Tris-HCl pH 7.5, 100 mM NaCl) and initial enzyme activity
425 was measured as described above. The enzymes were subsequently incubated at

426 temperatures from 30 °C to 54 °C for one hour using a PCR thermocycler machine
427 (Bio-Rad Laboratories, Hercules, CA, USA), followed by cooling for 10 minutes at
428 4 °C, incubation at RT for 10 minutes, and centrifugation for 2 min using a tabletop
429 centrifuge. The residual enzyme activity was measured as described above and recorded
430 as relative to the initial activity. The temperature where half of the initial activity was
431 lost was determined by four-parameter logistic regression using Prism 9 (GraphPad
432 Software, San Diego, CA, USA). The experiment was performed three times using two
433 different enzyme preparations, each time with three technical triplicates.
434
435 **Enzyme steady state kinetics**
436 To determine the K_M for TMA mFMO and mFMO_20 were purified essentially as
437 described above and flash frozen in 20% glycerol. 50 or 25 pmol of enzyme was diluted
438 in 880 µl reaction buffer (50 mM tris-HCl, pH 8.0) in a cuvette, and mixed with 20 µL
439 10 mM NADPH (final concentration: 200 µM). The enzyme and cofactor were
440 incubated for 2 minutes at room temperature before 50 µl TMA (final concentration
441 between 1-500 µM) was added to the cuvette. This was mixed thoroughly, and the
442 absorbance decrease at 340 nm was immediately measured for 2 minutes in a Cary 60
443 UV-Vis spectrophotometer (Agilent Technologies) at 23 °C to obtain the initial reaction
444 rate of the enzymes (V_0), defined as the change in absorbance per minute in the linear
445 part of the curve. To calculate the product formation per enzyme (µmol product min^{-1}
446 µmol $enzyme^{-1}$), the NADPH conversion rate was calculated from the absorbance
447 change assuming a molar extinction coefficient of NADPH of 6220 M^{-1} cm^{-1}. The
448 product formation per enzyme was plotted against the TMA concentration, and K_M and
449 k_{cat} were calculated using nonlinear regression in Prism 9. Each enzyme was expressed

450 and purified in two biological replicates, and for each biological replicate two replicate
451 measurements were made and averaged.
452
453 **CD spectroscopy**
454 Melting temperatures of the mFMO variants were recorded by circular dichroism (CD)
455 spectrometry essentially as previously described (Goris et al., 2020). Briefly, the
456 enzymes were diluted to 0.7-0.8 mg/mL in reaction buffer (50 mM Tris-HCl pH 7.5,
457 100 mM NaCl) and denaturation was monitored, using 0.1-
458 cm path length quartz cuvettes, at 220 nm between 10 °C and 95 °C at a rate of 30 °C
459 per hour using a Jasco J-720 spectropolarimeter (Japan Spectroscopic Corporation,
460 JASCO, Tokyo, Japan) equipped with a Peltier temperature controller. The melting
461 temperature was calculated by fitting the ellipticity (mdeg) at 220 nm for each of the
462 different temperatures using four-parameter logistic regression using Prism 9 (GraphPad
463 Software).
464
465 **Enzymatic conversion of TMA to TMAO in salmon protein hydrolysates**
466 Enzymatic conversion of TMA present in the salmon protein hydrolysate to TMAO was
467 performed essentially as described previously (Goris et al., 2020). The salmon protein
468 hydrolysate (64.4% dry weight) was produced from fresh salmon by-products by
469 protease treatment and provided by the Biomega Group (Skogsvåg, Norway). The
470 viscous salmon protein hydrolysate was diluted 1:5 (wt/vol) in ultrapure water, followed
471 by sonication in an ultrasonic water bath (J.P. Selecta, S.A., Barcelona, Spain) at 50 Hz
472 for 5 min, vortexing for 5 min, and centrifugation at 16,000 × *g* for 10 min. The
473 resulting supernatant (pH 6.10) was supplemented with 0.50 mM NADPH and

474 10 ng/mL mFMO or mFMO_20 enzyme and incubated for 1 h at 30 °C, 50 °C and 65
475 °C. The enzymatic reaction was stopped by diluting 10 times with methanol. All
476 reactions were performed with two technical triplicates using one enzyme preparation
477 and included control samples without enzyme. The TMA levels in the samples were
478 determined using Ultra High Performance Liquid Chromatography (UHPLC) with
479 EVOQ Elite Triple Quadrupole Mass Spectrometer (Bruker, Billerica, MA, USA), each
480 replicate measured two times. Prior to the analysis the samples were diluted 1:1000 by
481 mixing with methanol and subsequently vortexed for 1 min. TMA and TMAO standards
482 were prepared in water to a final concentration of 25, 50, 100, 200 and 250 ppb. A
483 liquid chromatography system consisting of a degasser, a binary pump, and an auto-
484 sampler (at 4 ºC) was used. Samples were applied to a column (Ace Excel 3, C18-
485 Amida, 3µm, 150 x 4.6mm ID; Advanced Chromatography Technologies Ltd., Reading,
486 UK), which was maintained at 40 °C during the analysis. The system was operated at a
487 flow rate of 0.5 mL/min with solvent A (H_2O containing 0.1% formic acid) and solvent
488 B (methanol). The system was held at 2% B for 7 min of total analysis time. Data were
489 collected in positive electrospray ionization (ESI) mode using Q-TOF (model Agilent
490 6120; Agilent Technologies). The spray voltage was 5000 V, the cone temperature 350
491 ºC, the cone gas flow 40 L/h, the heated probe temperature 400 ºC, the probe gas flow
492 50 L/h, and the nebulizer gas flow 60 L/h. The experiment was performed twice with
493 technical duplicates. The analyses were performed at the Servicio Interdepartamental de
494 Investigación (SIDI) from the Autonomous University of Madrid (analyses ID 200-
495 01807, 200-01761, and 200-01629).
496
497 **Crystallization of mFMO_20**

498 The complex of mFMO_20 with $NADP^+$ and FAD was obtained by co-crystallization
499 assays incubating 5.13 mg/ml protein in 20 mM Tris pH 8, 150 mM NaCl, 1 mM DTT
500 with 1 mM NADPH during 25 min at 4 ºC. Initial crystallization conditions were
501 explored by a NanoDrop robot (Innovadyne Technologies, Santa Rosa, CA, USA) and
502 the commercial screen Index (Hampton Research, Aliso Viejo, CA, USA). Yellow
503 prism bar shaped crystals were grown after two months by adding 250 nl of the protein
504 mixture to 250 nl of precipitant solution (2 M $(NH_4)_2SO_4$, 0.1 M Bis-Tris pH 6.5). For
505 data collection, crystals were transferred to a cryoprotectant solution consisting of 2.2
506 M $(NH_4)_2SO_4$, 0.1 M Bis-Tris pH 6.5 and 23% (v/v) glycerol, before being cooled in
507 liquid nitrogen.
508
509 **Data collection and structure determination**
510 Diffraction data were collected using synchrotron radiation on the XALOC beamline at
511 ALBA (Cerdanyola del Vallés, Spain). Diffraction images were processed with XDS
512 (Kabsch, 2010) and merged using AIMLESS from the CCP4 package (Evans and
513 Murshudov, 2013). The crystals were indexed in the $C222_1$ space group, with two
514 molecules in the asymmetric unit and 44% solvent content within the cell. The structure
515 of mFMO_20 complexed with NADPH was solved by Molecular Replacement with
516 MOLREP (Vagin and Teplyakov, 2010) using the coordinates from the wild type as
517 template (PDB ID: 2XVE). Crystallographic refinement was performed using the
518 program REFMAC (Murshudov et al., 1997) within the CCP4 suite with local non-
519 crystallographic symmetry (NCS). A summary of the data collection and refinement
520 statistics is found in Table S1. Free R-factor was calculated using a subset of 5%
521 randomly selected structure-factor amplitudes that were excluded from automated

522 refinement. At the later stages, ligands were manually built into the electron density
523 maps with COOT (Emsley et al., 2010) and water molecules were included in the
524 model, and combined with more rounds of restrained refinement. The figures were
525 generated with PyMOL. The structure is available with PDB ID 8B2D.

526

527 **Identification of polar interactions**

528 To perform an inclusive identification of salt bridges in both the native mFMO (PDB
529 ID: 2XVH) and mFMO_20 structures, MolProbity (Williams et al., 2018) was used to
530 add hydrogen atoms and optimize polar contacts by side-chain flip correction of Asn,
531 Gln, and His residues. Residues that were flipped in both structures were Q17, Q40,
532 N48, H164, and N282, additional residues flipped in mFMO were Q25, Q143, and
533 N290, and residues flipped only in mFMO_20 were H128, M353Q, Q377, and H414.
534 Chain A from these optimized structures were used to identify salt bridges with the
535 VMD Salt Bridges Plugin (as described above). PyMOL was used to confirm the
536 predicted salt bridges, to identify additional hydrogen bonds involving mutated
537 residues, and to visualize the structural models.

538

539

540 Acknowledgments

541 Authors would like to acknowledge Sergio Ciordia at the Proteomic Facilities from the
542 CSIC-CNB (that belongs to ProteoRed, PRB2-ISCIII, supported by Grant PT13/0001)
543 for the MALDI-TOF/TOF analyses, Rosa Sedano and Eva Martín at the Servicio
544 Interdepartamental de Investigación (SIDI) from the Autonomous University of Madrid
545 for the UHPLC-MS analyses, and Ruth Matesanz from the CSIC-CIB for her support

for CD analyses. G.E.K.B gratefully acknowledge funding from the Research Council of Norway with an additional mobility grant to M.G. (RCN grant number 280737) as well as funding from the European Union's Horizon 2020 research and innovation programme under grant agreement No 101000607. M.F. and J-S.A. acknowledge the European Union's Horizon 2020 research and innovation programme under grant agreement No 101000327, and the financial support under Grants PID2020-112758RB-I00 (M.F.), PDC2021-121534-I00 (M.F.) and PID2019-105838RB-C33 (J.S-A.) from the Ministerio de Ciencia e Innovación, Agencia Estatal de Investigación (AEI) (Digital Object Identifier 10.13039/501100011033), Fondo Europeo de Desarrollo Regional (FEDER) and the European Union ("NextGenerationEU/PRTR"), and Grant 2020AEP061 (M.F.) from the Agencia Estatal CSIC. J-S.A. and I.C-R., thank the staff of the Synchrotron Radiation Source at Alba (Barcelona, Spain) for assistance at BL13-XALOC beamline. G.E.K.B. and M.G. would like to thank M.F. and CSIC for hosting the mobility stay. Authors thank Bjørn Liaset at the Biomega Group for providing salmon protein hydrolysate.

Author contributions

G.E.K.B. and P.P. performed the PROSS analysis. M.G. planned experiments, cloned and purified all constructs, conducted biochemical experiments and analyzed all data. I.C.R. and J.S-A. conducted crystallography and structural analysis. R.R. conducted kinetic analyses. D.A. conducted CD experiments. M.F. supervised and prepared all mass spectrometry experiments together with M.G. G.E.K.B. secured the main funding, conceptualized the study, and supervised the project together with P.P. and M.F. M.G.

and P.P. wrote the paper with input from I.C.R., J.S-A., R.R., M.F., and G.E.K.B. All authors read and revised the manuscript.

Competing interests

The authors declare no conflict of interest.

Data Availability

Coordinates and structure factors have been deposited in the Protein Data Bank under PDB accession code 8B2D.

References

Alfieri A, Malito E, Orru R, Fraaije MW, Mattevi A. 2008. Revealing the moonlighting role of NADP in the structure of a flavin-containing monooxygenase. *Proc Natl Acad Sci U S A* **105**:6572–7. doi:10.1073/pnas.0800859105

Aspevik T, Egede-Nissen H, Oterhals Ĺ. 2016. A Systematic Approach to the Comparison of Cost Efficiency of Endopeptidases for the Hydrolysis of Atlantic Salmon (Salmo salar) By-Products. *Food Technol Biotechnol* **54**:421–431. doi:10.17113/ftb.54.04.16.4553

Bjerga GEK, Arsın H, Larsen Ø, Puntervoll P, Kleivdal HT. 2016. A rapid solubility-optimized screening procedure for recombinant subtilisins in E. coli. *J Biotechnol* **222**:38–46. doi:10.1016/j.jbiotec.2016.02.009

Ceccoli RD, Bianchi DA, Rial D V. 2014. Flavoprotein monooxygenases for oxidative biocatalysis: recombinant expression in microbial hosts and applications. *Front Microbiol* **5**:25. doi:10.3389/fmicb.2014.00025

593 Chen Y, Patel NA, Crombie A, Scrivens JH, Murrell JC. 2011. Bacterial flavin-
594 containing monooxygenase is trimethylamine monooxygenase. *Proc Natl Acad Sci*
595 *U S A* **108**:17791–6. doi:10.1073/pnas.1112928108
596 Cho HJ, Cho HY, Kim KJ, Kim MH, Kim SW, Kang BS. 2011. Structural and
597 functional analysis of bacterial flavin-containing monooxygenase reveals its ping-
598 pong-type reaction mechanism. *J Struct Biol* **175**:39–48.
599 doi:10.1016/j.jsb.2011.04.007
600 Choi HS, Kim JK, Cho EH, Kim YC, Kim J Il, Kim SW. 2003. A novel flavin-
601 containing monooxygenase from *Methylophaga* sp strain SK1 and its indigo
602 synthesis in *Escherichia coli*. *Biochem Biophys Res Commun* **306**:930–6.
603 doi:10.1016/s0006-291x(03)01087-8
604 Emsley P, Lohkamp B, Scott WG, Cowtan K. 2010. Features and development of Coot.
605 *Acta Crystallogr D Biol Crystallogr* **66**:486–501.
606 doi:10.1107/S0907444910007493
607 Evans PR, Murshudov GN. 2013. How good are my data and what is the resolution?
608 *Acta Crystallogr D Biol Crystallogr* **69**:1204–14.
609 doi:10.1107/S0907444913000061
610 Fabara AN, Fraaije MW. 2020. An overview of microbial indigo-forming enzymes.
611 *Appl Microbiol Biotechnol* **104**:925–933. doi:10.1007/s00253-019-10292-5
612 Fürst MJLJ, Boonstra M, Bandstra S, Fraaije MW. 2019. Stabilization of
613 cyclohexanone monooxygenase by computational and experimental library design.
614 *Biotechnol Bioeng* **116**:2167–2177. doi:10.1002/bit.27022
615 Geertsma ER, Dutzler R. 2011. A versatile and efficient high-throughput cloning tool
616 for structural biology. *Biochemistry* **50**:3272–8. doi:10.1021/bi200178z

617 Goldenzweig A, Goldsmith M, Hill SE, Gertman O, Laurino P, Ashani Y, Dym O,
618 Unger T, Albeck S, Prilusky J, Lieberman RL, Aharoni A, Silman I, Sussman JL,
619 Tawfik DS, Fleishman SJ. 2016. Automated Structure- and Sequence-Based
620 Design of Proteins for High Bacterial Expression and Stability. *Mol Cell* **63**:337–
621 346. doi:10.1016/j.molcel.2016.06.012
622 Goris M, Puntervoll P, Rojo D, Claussen J, Larsen Ø, Garcia-Moyano A, Almendral D,
623 Barbas C, Ferrer M, Bjerga GEK. 2020. Use of Flavin-Containing
624 Monooxygenases for Conversion of Trimethylamine in Salmon Protein
625 Hydrolysates. *Appl Environ Microbiol* **86**. doi:10.1128/AEM.02105-20
626 Han GH, Gim GH, Kim W, Seo S Il, Kim SW. 2012. Enhanced indirubin production in
627 recombinant *Escherichia coli* harboring a flavin-containing monooxygenase gene
628 by cysteine supplementation. *J Biotechnol* **164**:179–87.
629 doi:10.1016/j.jbiotec.2012.08.015
630 Hebard C, Flick G, Martin R. 1982. Occurrence and significance of trimethylamine
631 oxide and its derivatives in fish and shellfish. Chemistry and Biochemistry of
632 Marine Food Products. AVI Publishing Group, Westport, CT. pp. 149–304.
633 Kabsch W. 2010. XDS. *Acta Crystallogr D Biol Crystallogr* **66**:125–32.
634 doi:10.1107/S0907444909047337
635 Klesmith JR, Bacik J-P, Wrenbeck EE, Michalczyk R, Whitehead TA. 2017. Trade-offs
636 between enzyme fitness and solubility illuminated by deep mutational scanning.
637 *Proc Natl Acad Sci U S A* **114**:2265–2270. doi:10.1073/pnas.1614437114
638 Kristinsson HG, Rasco BA. 2000. Fish protein hydrolysates: production, biochemical,
639 and functional properties. *Crit Rev Food Sci Nutr* **40**:43–81.
640 doi:10.1080/10408690091189266

641 Lončar N, van Beek HL, Fraaije MW. 2019. Structure-Based Redesign of a Self-
642 Sufficient Flavin-Containing Monooxygenase towards Indigo Production. *Int J*
643 *Mol Sci* **20**. doi:10.3390/ijms20246148
644 Mourelle-Insua Á, Aalbers FS, Lavandera I, Gotor-Fernández V, Fraaije MW. 2019.
645 What to sacrifice? Fusions of cofactor regenerating enzymes with Baeyer-Villiger
646 monooxygenases and alcohol dehydrogenases for self-sufficient redox biocatalysis.
647 *Tetrahedron* **75**:1832–1839. doi:10.1016/j.tet.2019.02.015
648 Murshudov GN, Vagin AA, Dodson EJ. 1997. Refinement of macromolecular
649 structures by the maximum-likelihood method. *Acta Crystallogr D Biol*
650 *Crystallogr* **53**:240–55. doi:10.1107/S0907444996012255
651 Peleg Y, Vincentelli R, Collins BM, Chen K-E, Livingstone EK, Weeratunga S, Leneva
652 N, Guo Q, Remans K, Perez K, Bjerga GE., Larsen Ø, Vaněk O, Skořepa O,
653 Jacquemin S, Poterszman A, Kjær S, Christodoulou E, Albeck S, Dym O,
654 Ainbinder E, Unger T, Schuetz A, Matthes S, Bader M, de Marco A, Storici P,
655 Semrau MS, Stolt-Bergner P, Aigner C, Suppmann S, Goldenzweig A, Fleishman
656 SJ. 2021. Community-Wide Experimental Evaluation of the PROSS Stability-
657 Design Method. *J Mol Biol* **433**:166964. doi:10.1016/j.jmb.2021.166964
658 Rioz-Martínez A, Kopacz M, de Gonzalo G, Torres Pazmiño DE, Gotor V, Fraaije MW.
659 2011. Exploring the biocatalytic scope of a bacterial flavin-containing
660 monooxygenase. *Org Biomol Chem* **9**:1337–41. doi:10.1039/c0ob00988a
661 Santiago G, Martínez-Martínez M, Alonso S, Bargiela R, Coscolín C, Golyshin PN,
662 Guallar V, Ferrer M. 2018. Rational Engineering of Multiple Active Sites in an
663 Ester Hydrolase. *Biochemistry* **57**:2245–2255. doi:10.1021/acs.biochem.8b00274
664 Schmidt AC, Leroux J-C. 2020. Treatments of trimethylaminuria: where we are and

665 where we might be heading. *Drug Discov Today* **25**:1710–1717.
666 doi:10.1016/j.drudis.2020.06.026
667 Shavandi A, Hou Y, Carne A, McConnell M, Bekhit AE-DA. 2019. Marine Waste
668 Utilization as a Source of Functional and Health CompoundsAdvances in Food and
669 Nutrition Research. pp. 187–254. doi:10.1016/bs.afnr.2018.08.001
670 Torres Pazmiño DE, Winkler M, Glieder A, Fraaije MW. 2010. Monooxygenases as
671 biocatalysts: Classification, mechanistic aspects and biotechnological applications.
672 *J Biotechnol* **146**:9–24. doi:10.1016/j.jbiotec.2010.01.021
673 Vagin A, Teplyakov A. 2010. Molecular replacement with MOLREP. *Acta Crystallogr*
674 *D Biol Crystallogr* **66**:22–5. doi:10.1107/S0907444909042589
675 van Berkel WJH, Kamerbeek NM, Fraaije MW. 2006. Flavoprotein monooxygenases, a
676 diverse class of oxidative biocatalysts. *J Biotechnol* **124**:670–89.
677 doi:10.1016/j.jbiotec.2006.03.044
678 Villamil O, Váquiro H, Solanilla JF. 2017. Fish viscera protein hydrolysates:
679 Production, potential applications and functional and bioactive properties. *Food*
680 *Chem* **224**:160–171. doi:10.1016/j.foodchem.2016.12.057
681 Wijma HJ, Fürst MJLJ, Janssen DB. 2018. A Computational Library Design Protocol
682 for Rapid Improvement of Protein Stability: FRESCO. *Methods Mol Biol* **1685**:69–
683 85. doi:10.1007/978-1-4939-7366-8_5
684 Williams CJ, Headd JJ, Moriarty NW, Prisant MG, Videau LL, Deis LN, Verma V,
685 Keedy DA, Hintze BJ, Chen VB, Jain S, Lewis SM, Arendall WB, Snoeyink J,
686 Adams PD, Lovell SC, Richardson JS, Richardson DC. 2018. MolProbity: More
687 and better reference data for improved all-atom structure validation, *Protein Sci.*
688 **27**: 293–315. doi:10.1002/pro.3330

689

690 # Tables

691 **Table 1. Predicted new salt bridges formed between mutated residues and native or**
692 **mutated residues.** Empty cells indicate the absence of the mutated residue listed to the
693 left. Residues (native or mutant) forming a predicted salt bridge with the mutant residue
694 (left column) are listed, and if a mutant residue does not form a salt bridge in an mFMO
695 variant, it is marked by a minus (-). The total number of mutant residues involved in
696 forming salt bridges are shown in the bottom row.

Mutated residue	Mutant mFMO variant						
	mFMO_8	mFMO_11	mFMO_14	mFMO_15	mFMO_20	mFMO_24	mFMO_28
N290D			R292	R292	R292	R292	R292
M353K	E357	E357					
K358R			D374	D374	D374	D374	D374
L360E			-	-	-	-	R356/R292
A365D					K401	K401	K401
T370D	-	-	-	-	-	N394K	N394K
N378D	K300	K300	K300	K300	K300	K300	K300
P391D							N394K
N394K						T370D/D374	T370D/D374/P391D
L398K		E366	E366	E366	E366	E366	-
Total	**2**	**3**	**4**	**4**	**5**	**7**	**8**

697

698

699 **Table 2. Predicted interhelical salt bridges involving or induced by mutated residues**
700 **in PROSS mutant models**. Note that the α6-β18/β19-α7 salt bridge connects helices α6
701 and α7 via the β18/β19 loop and that the α6-β17/β18 salt bridge connects helix α6 to the
702 β17/β18 loop.

mFMO variant	Interhelical salt bridges				
	α6-α7	α6-β18/β19-α7	α7-α8	α6-β17/β18	Total
mFMO_8		D351-K300-N378D			1
mFMO_11		D351-K300-N378D	E366-L398K		2
mFMO_14	K358R-D374	D351-K300-N378D	E366-L398K		3
mFMO_15	K358R-D374	D351-K300-N378D	E366-L398K		3
mFMO_20	K358R-D374	D351-K300-N378D	E366-L398K; A365D-K401		4
mFMO_24	K358R-D374	D351-K300-N378D	E366-L398K; A365D-K401; T370D-N394K; D374-N394K		6
mFMO_28	K358R-D374	D351-K300-N378D	A365D-K401; T370D-N394K; D374-N394K	L360E-R292	6

703

704

705

706 **Table 3. Biochemical parameters of mFMO and mutant variants.**

707 Melting curves were obtained by CD at pH 7.5 and the melting temperature (T_m ± 95%
708 CI) was estimated by four-parameter logistic regression of the melting curve.
709 Temperature where half enzyme activity is lost ($T_{1/2}$) was measured at pH 7.5 and the
710 reported values are means of three independent experiments (± SD). Optimal temperature
711 (T_{opt}) was determined at pH 8.0 for mFMO and mFMO_20. Optimal pH for TMA
712 conversion was determined at 22 °C. Steady-state kinetic measurements were performed
713 with varying concentrations of TMA (Sigma-Aldrich) as the substrate with fixed NADPH
714 concentration (200 μM) at 23°C, pH 8.0. Reported values are the means of two biological
715 replicates (± SD).

Enzyme	T_m (°C)	$T_{1/2}$ (°C)	T_{opt} (°C)	Optimal pH	K_M (μM)	k_{cat} (s^{-1})	k_{cat}/K_M (μM^{-1} s^{-1})
mFMO	46.2±0.2	40.6±0.4	40	8.5	1.07±0.13	1.28±0.03	1.20±0.12
mFMO_8	51.2±0.1	45.1±0.9	-	7.5	-	-	-
mFMO_11	51.7±0.1	47.1±1.2	-	7.5	-	-	-
mFMO_14	53.9±0.2	49.0±1.5	-	8.0	-	-	-
mFMO_15	54.5±0.1	49.6±0.4	-	7.5	-	-	-
mFMO_20	55.2±0.1	50.0±0.4	40	8.0	0.83±0.02	0.93±0.05	1.11±0.03
mFMO_24	52.0±0.1	49.2±0.2	-	7.5	-	-	-
mFMO_28	50.9±0.1	48.9±0.5	-	8.0	-	-	-

716

717

718 **Table 4. New polar interactions directly involving or induced by side chain atoms of**

719 **mutated residues in mFMO_20.** Hydrogen donor and acceptor atoms of the amino acid

720 side chains are indicated in parenthesis, the distances between them are shown, and the

721 structural location is indicated by secondary structure element.

Hydrogen donor	Hydrogen acceptor	Distance (Å)	Structural location	
			Donor	Acceptor
K300 (N^{ζ})	D351 ($O^{\delta2}$)	3.0	loop β18-β19	α6
K300 (N^{ζ})	N378D ($O^{\delta2}$)	2.8	loop β18-β19	α7
R356 (N^{ε}/$N^{\eta2}$)	M353Q ($O^{\varepsilon1}$)	2.8/2.7	α6	α6
R356 ($N^{\eta1}$)	L360E ($O^{\varepsilon2}$)	3.4	α6	α6
K358R ($N^{\eta1}$/$N^{\eta2}$)	D374 ($O^{\delta2}$)	3.0/2.8	α6	α7
N394 ($N^{\delta2}$)	T370D ($O^{\delta1}$)	3.4	α8	α7
L398K (N^{ζ})	E366 ($O^{\varepsilon2}$)	3.1	α8	α7
K401 (N^{ζ})	A365D ($O^{\delta2}$)	2.7	α8	α7

722

723

724 **Figures**

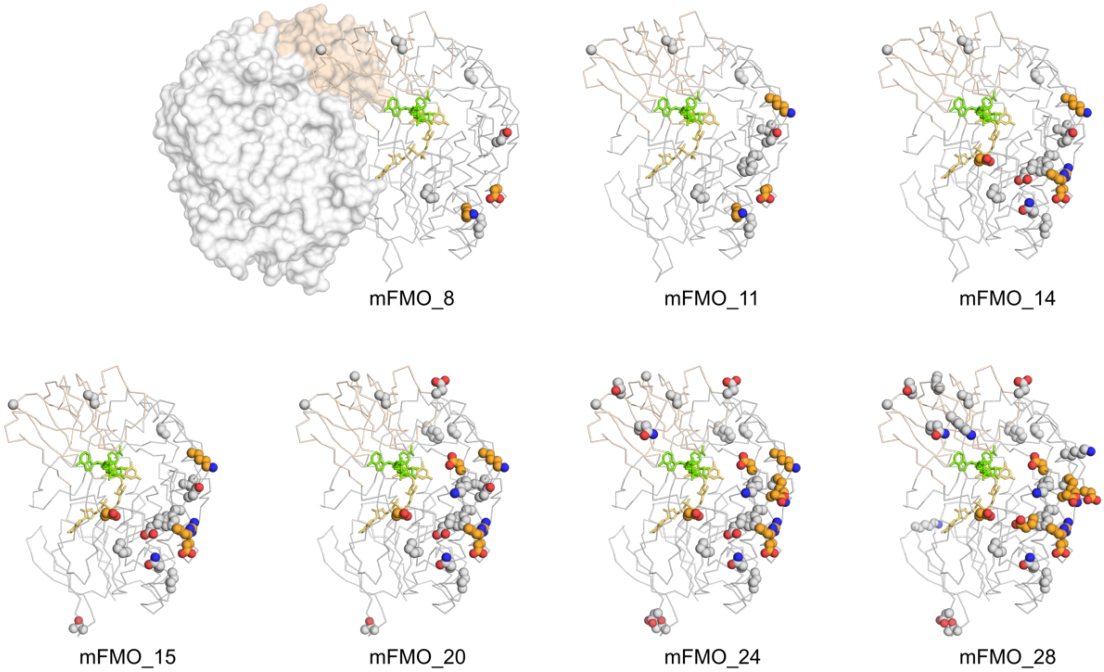

725

726 **Figure 1. Structural models of mFMO and mutant variants.** The structural models of
727 the 7 variants of mFMO with 8 to 28 mutations (top left to bottom right), as generated by
728 PROSS (using PDB:2XVH), are shown in ribbon view (chain A only). For context and
729 to indicate the dimer interface, chain B of native mFMO is shown in surface view (top
730 left, PDB:2XVH). The large domain is shown in grey, the small domain in wheat, and the
731 cofactors FAD and $NADP^+$ are shown in yellow and green sticks, respectively. Mutant
732 residues predicted to form salt bridges are shown as orange spheres, and other mutations
733 are shown as grey spheres. Nitrogen and oxygen atoms of the mutant residues are colored
734 blue and red, respectively.

735

736

737

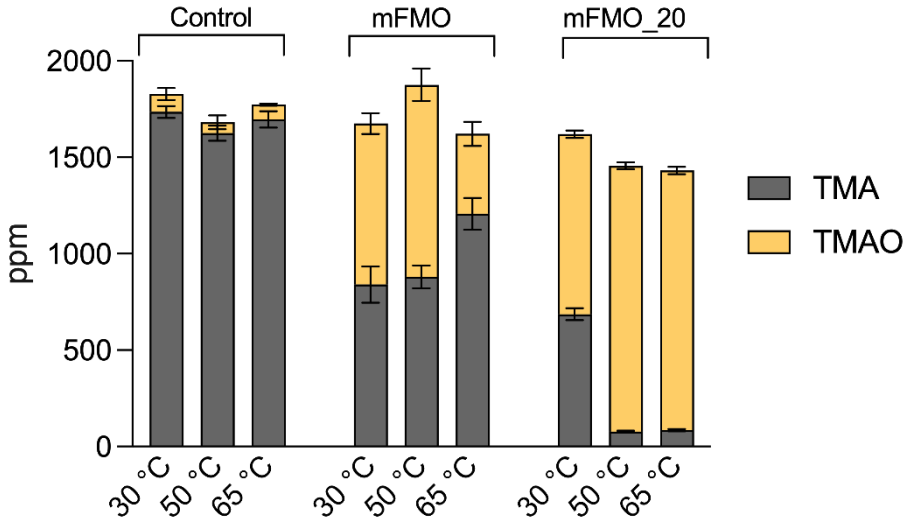

738

739 **Figure 2. Enzymatic TMA conversion in salmon protein hydrolysate.** Salmon protein
740 hydrolysates (pH 6.1) were incubated for 1 hour at 30, 50 and 65 °C with no enzyme
741 (control), mFMO, or mFMO_20, all supplemented with 0.5 mM NADPH. TMA and
742 TMAO levels were determined using UHPLC with EVOQ Elite Triple Quadrupole Mass
743 Spectrometer. The experiment was performed twice, each time with three technical
744 replicates, and the plot shows the mean TMA (grey) and TMAO (yellow) levels (ppm) in
745 stacks with standard deviations represented by error bars.

746

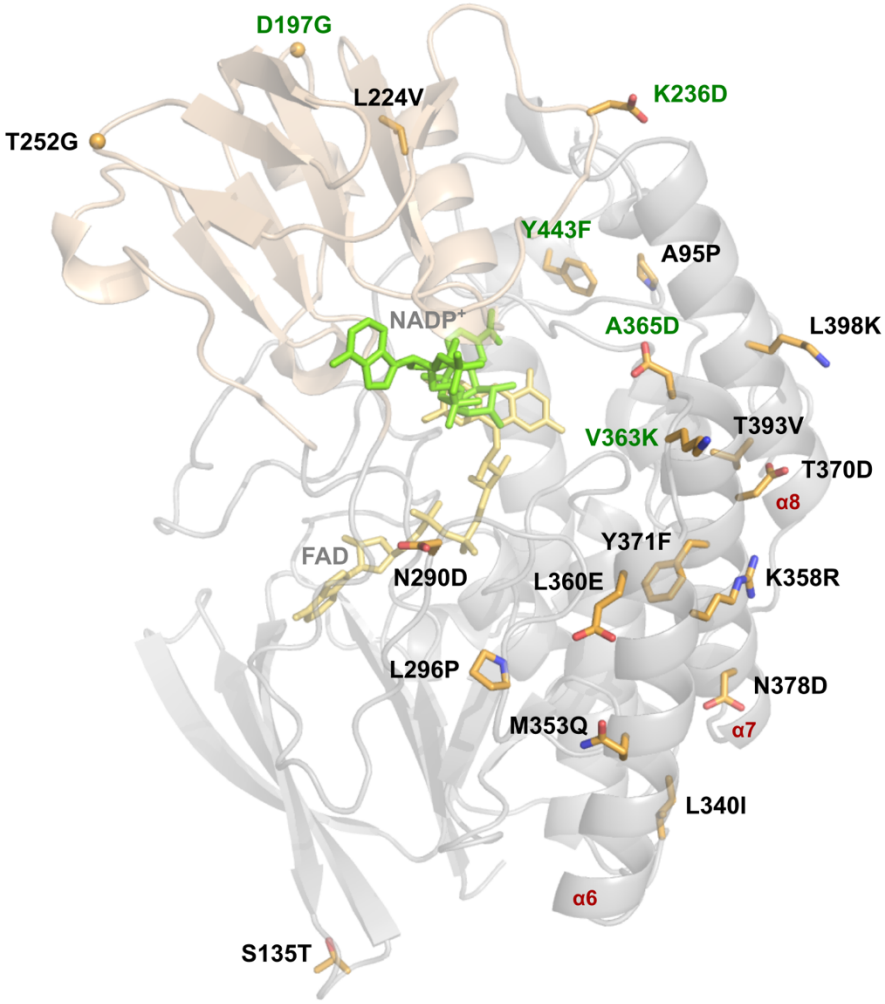

747

748 **Figure 3. Crystal structure of mFMO_20.** The structure of the mFMO_20 monomer
749 (PDB ID: 8B2D) (chain A) is shown as cartoon, with the large domain colored in gray
750 and the small domain colored in wheat. The cofactors FAD and $NADP^+$ are shown as
751 yellow and green sticks, respectively. The side chains of the 20 mutated residues are
752 represented as orange sticks, and oxygen and nitrogen atoms colored red and blue,
753 respectively. The alpha carbons of the introduced glycine residues are shown as spheres.
754 The 5 residues that are new compared to mFMO_15 are labeled in green. The three α-
755 helices where the 10 of 20 mutated residues are located are labeled in red.

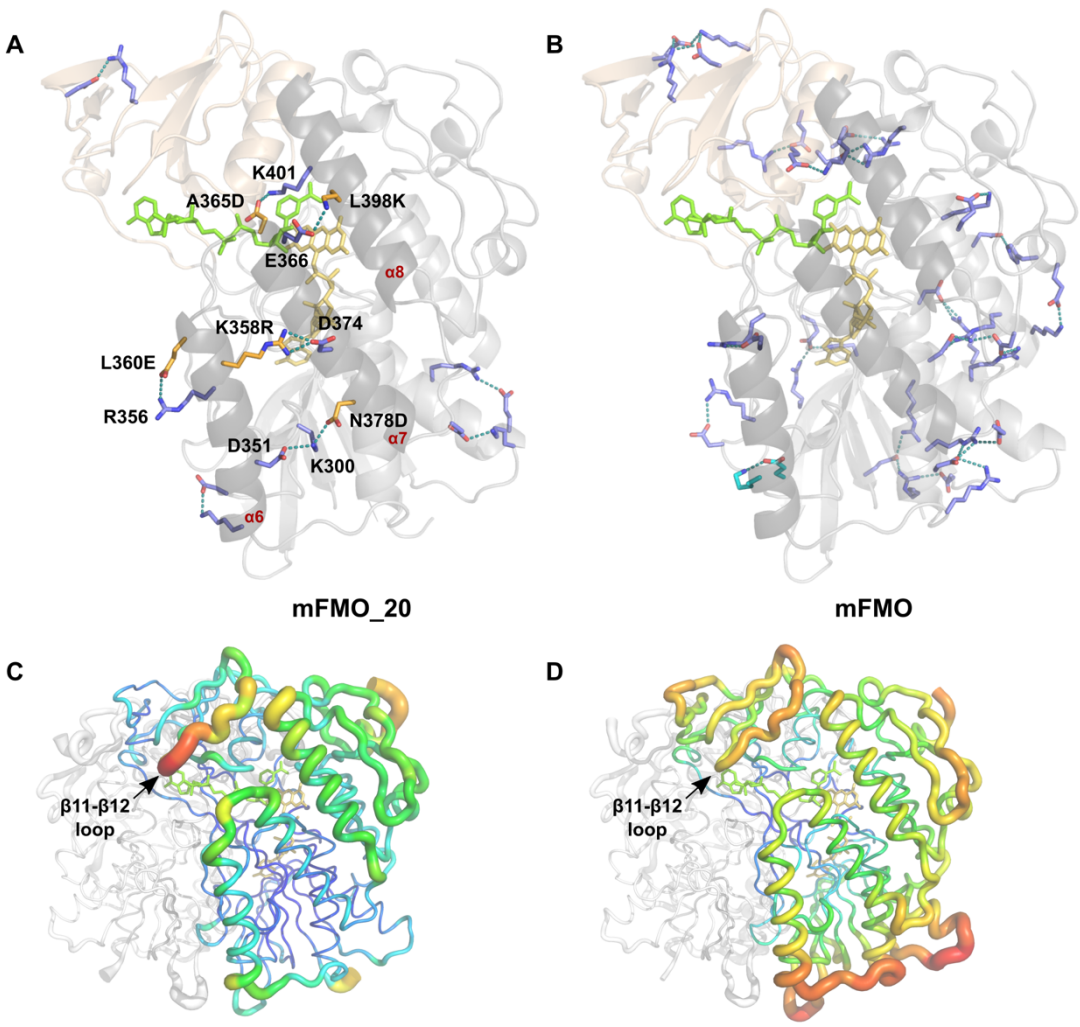

Figure 4. Stabilizing salt bridges in native mFMO and mutant mFMO_20. A) Chain A of the mFMO_20 structure is shown as cartoon, the small and large domains are colored in wheat and gray, respectively, and the cofactors FAD and $NADP^+$ are shown as yellow and green sticks, respectively. Residues forming salt bridges that are unique to mFMO_20 are shown as sticks, hydrogen bonds between interacting residues are shown as teal-colored dashes, and oxygen and nitrogen atoms are colored red and blue, respectively. Native and mutated residues are colored blue and orange, respectively. The residues of

765 salt bridges involving mutant residues are labeled. The three α-helices where the mutated
766 residues are located are labeled in red. **B)** Chain A of the mFMO structure (PDB ID
767 2XVH) is visualized essentially as in A. Residues that form salt bridge pairs in both the
768 native mFMO and mutant mFMO_20 are colored slate blue, and the lone pair which is
769 unique to mFMO is colored cyan. **C)** The biological dimer of native mFMO is shown in
770 B-factor putty representation. Red colors and large diameters of the tube indicate flexible
771 regions with higher B-factors, in contrast to blue colors with small diameters, indicating
772 well-ordered regions with lower B-factors. The location of the loop between β-strands 11
773 and 12 is indicated. Chain B is colored white. **D)** The biological dimer of mutant
774 mFMO_20 is visualized as in C. The view of all structures has been rotated -60° around
775 the y-axis compared to Figure 3.

776